catalysts

MDPI

Article

Insights into the Three-Component Coupling Reactions of Aldehydes, Alkynes, and Amines Catalyzed by N-heterocyclic Carbene Silver: A DFT Study

Chenggen Zhang [1,*], Shuyuan Yu [1,2], Fei Wang [1], Jian Cao [1,*], Xinru Liang [1], Fuping Wang [1], Huimin Zheng [1], Yaning Zhang [1], Mengyao Yang [1] and Boyu Zhao [1]

[1] College of Chemistry and Material Science, Langfang Normal University, Langfang 065000, China; yushuyuan05@mails.ucas.ac.cn (S.Y.)
[2] College of Chemistry and Chemical Engineering, University of Chinese Academy of Sciences, Beijing 100049, China
* Correspondence: chgzhang04@mails.ucas.ac.cn (C.Z.); caojian@lfnu.edu.cn (J.C.)

Abstract: Density functional theory (DFT) was used to investigate the three-component coupling reactions of aldehydes, alkynes, and amines (A3 coupling) using N-heterocyclic carbene silver as the catalyst. This study reveals that the addition reaction between the catalyst N-heterocyclic carbene silver and phenylacetylene (PAE) forms Ag_PAE. Subsequently, one hydrogen atom of the Ag_PAE migrates to the nitrogen atom of the Amine. Thereafter, the amine aldehyde condensation reaction generates a molecule of water and an imine ion with (Path one) or without (Path two) another amine catalyst. Path one has a lower reaction barrier than Path two. Subsequently, the imine ion reacts with silver phenylacetylide to generate the A3 coupling reaction product propargylamine (PPA). Furthermore, the triple bond and $-N_3$ group in PPA undergo a cycloaddition reaction and generate the final product (PR). The entire reaction is strongly exothermic, and, therefore, the reaction is easy to conduct. Moreover, conceptual density functional theory calculations confirm the reaction mechanism. Investigating the mechanism of these reactions will be helpful for understanding and developing new synthesis strategies for similar functional compounds.

Keywords: A3 coupling reaction; N-heterocyclic carbene silver; reaction mechanism; DFT calculations

check for updates

Citation: Zhang, C.; Yu, S.; Wang, F.; Cao, J.; Liang, X.; Wang, F.; Zheng, H.; Zhang, Y.; Yang, M.; Zhao, B. Insights into the Three-Component Coupling Reactions of Aldehydes, Alkynes, and Amines Catalyzed by N-heterocyclic Carbene Silver: A DFT Study. *Catalysts* **2023**, *13*, 646. https://doi.org/10.3390/catal13040646

Academic Editors: Maria Jaworska and Piotr Lodowski

Received: 12 February 2023
Revised: 15 March 2023
Accepted: 20 March 2023
Published: 23 March 2023

Copyright: © 2023 by the authors. Licensee MDPI, Basel, Switzerland. This article is an open access article distributed under the terms and conditions of the Creative Commons Attribution (CC BY) license (https://creativecommons.org/licenses/by/4.0/).

1. Introduction

Propargylamines (PPAs) are nitrogenous compounds with unique chemical structures and extensive applications. They can be used as important intermediates to create a variety of bioactive molecules and are widely used in organic synthesis, pharmaceutical chemistry, and other fields [1–3].

Multicomponent reactions are economical, selective, and energy-efficient [4]. Transition metal catalysts exhibit strong reaction activity, high selectivity, and chemical stability. The synthesis of PPAs through a three-component coupling reaction of aldehyde, acetylene, and amines catalyzed by transition metals is an efficient and atomic-economic method [5]. This type of reaction is also known as the A3 (alkyne, aldehyde, and amine) coupling reaction and has been extensively researched [6].

In 1998, McNally [7] and Dyatkin [8] reported the preparation of PPAs via the reactions of aldehydes, acetylene, and secondary amines in the presence of a catalytic amount (10 mol %) of CuCl as the catalyst; the yield of the product was between 70% and 90% with different substituents. In 2002, Li et al. reported the reactions of phenylacetylene (PAE), aldehydes, and aromatic primary amines cocatalyzed by $RuCl_3$ and CuBr [9]. When only CuBr was used as the catalyst, the reaction yield was extremely low; however, when $RuCl_3$ (3 mol %) and CuBr (30 mol %) were used as cocatalysts, the reaction yield was significantly improved from 30% to 90%.

In 2004, Shi et al. reported a rapid and microwave-assisted CuI (15 mol %) -catalyzed A3 coupling method, which involves microwave heating using water as a solvent; the yield of the product ranged from 41% to 93%, and this method has wide substrate applicability [10]. Yadav et al. used an ionic liquid as a solvent and CuBr as a catalyst for the A3 coupling reaction. This reaction can be performed using aromatic primary amines as well as fatty primary amines [11]. Subsequently, Eycken et al. used CuBr (20 mol %) as a catalyst to realize the A3 coupling reaction between an aliphatic primary amine substrate and terminal alkynes and aldehydes under microwave irradiation conditions, resulting in a significant shortening of the reaction time; the yield of the product ranged from 41% to 94% [12].

In 2014, Khanna et al. found that when the pyridine ring in the primary amine substrate was replaced with a benzimidazole ring during the cocatalysis of Cu(I) and Ag(I), the intramolecular cyclization/oxidation of PPA intermediates occurred to generate pyrimidine benzimidazole compounds [13]. Singh et al. used ortho-ester-substituted benzaldehyde substrates to react with terminal alkynes and primary amines via A3 coupling reactions using Cu(I) and chiral ligands as catalysts to generate chiral propargyl amines, followed by intramolecular internal amidation to generate optically active isoindoline ketones [14].

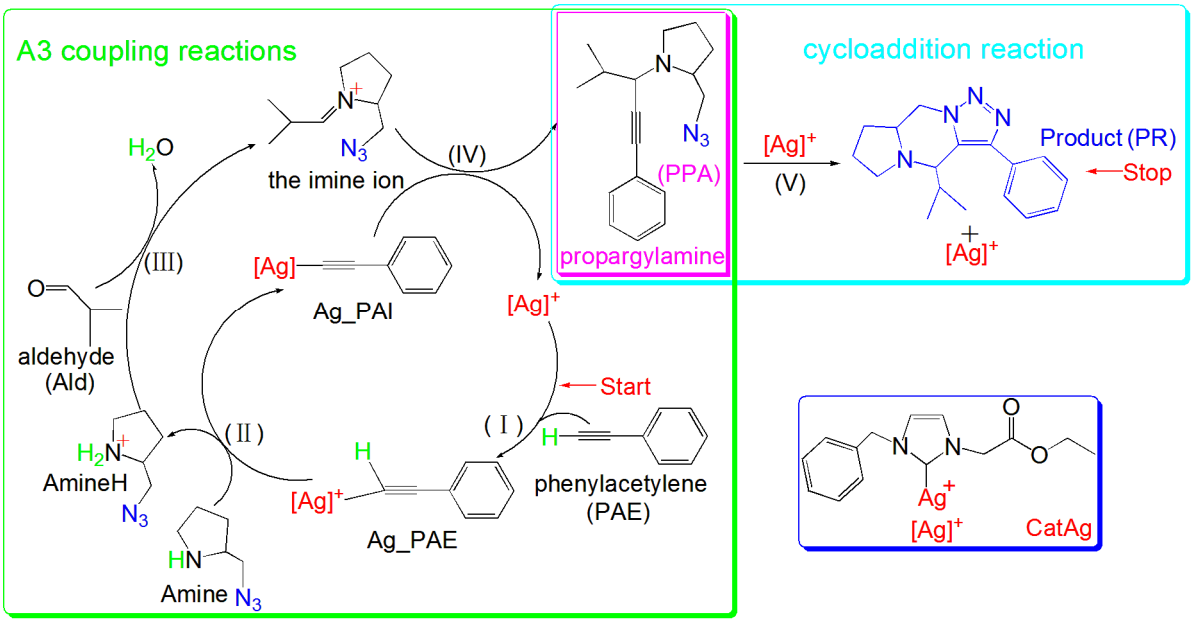
Transition metal compounds are widely used as catalysts to promote organic reactions because of their rich variety and good catalytic activity. The three-component A3 coupling reaction employing Cu salt as the catalyst was first used to promote the synthesis of PPA and other products. Subsequently, many reports have been published on the use of various transition metal catalysts, such as Ag [15–19], Au [20–22], Cu [23–25], In [26,27], Fe [28–30], Ni [31,32], and Pd [33], to promote this three-component reaction.

In 2014, Trose et al. synthesized pyridine-containing ligand silver(I) catalysts (3 mol %) and found that they could catalyze A3 coupling reactions under dielectric heating conditions, with the product yields ranging between 53% and 98% [15]. In 2018, Cao et al. found that polyacrylonitrile fiber-supported Au catalysts (1 mol %) could be used to synthesize secondary PPAs with short retention times and efficient productivity, and they achieved a product yield up to 86% [20]. In 2020, Nouruzi et al. prepared a covalent organic polymer Au catalyst (0.8 mol %) with a high activity for A3 coupling reactions and attained a product yield up to 90% [34]. Li et al. synthesized 2,4-disubstituted cyclopentenones using the A3 coupling method, where the addition of acidic 2,2,2-trifluoroethanol (TFE) as the reaction solvent was important for ensuring successful reactions [35]. In 2021, Xu et al. applied a microwave-assisted A3 coupling reaction to catalyze the reaction between two amines (formaldehyde and propionic acid) using Cu(I) (30 mol %) and attained a maximum product yield of 88%. Asymmetric 1, 4-diamino-2-butylene can be efficiently synthesized through a domino process [36].

In 2022, Cao synthesized a heterogeneous catalyst CuO–CeO_2 for the activation of terminal alkynes to promote cyclization/A3 coupling reactions. The results showed that the CuO–CeO_2 catalyst exhibited a good cycle performance and group compatibility in the A3 coupling reaction [37]. Kumar et al. synthesized three-dimensional architectures of silver(I)-based coordination polymers that could be used as catalysts for A3 coupling reactions [38]. Costabile et al. synthesized and tested A3-coupling reactions using silver and gold as catalysts (3 mol %). The maximum yields of the products were 88% for the silver catalyst and 90% for the gold catalyst. In addition, the catalytic behaviors of the two gold complexes with different substituents were compared using density functional theory (DFT) calculations. The results showed that both gold complexes had low transition state barriers for alkyne deprotonation [39].

In 2017, Cao et al. prepared recoverable N-heterocyclic carbene silver (**CatAg**) catalysts (0.5 mol %) to synthesize PPA; **CatAg** has high activity and can efficiently perform A3 coupling reactions. Additionally, the triple bond and $-N_3$ group in PPA underwent a cycloaddition reaction to generate the final product (PR) with a maximum product yield of 92% [40]. However, the specific reaction mechanism remains unclear, and to the best of our knowledge, no theoretical research has been conducted on the A3 coupling reactions

catalyzed by **CatAg**. Therefore, this study employed DFT calculations to investigate the catalytic mechanism of the A3 coupling reaction catalyzed by **CatAg**. Detailed research on the experimental mechanism will help us to understand the catalytic mechanism and provide new strategies for the synthesis of propargylamines. Scheme 1 shows a flowchart of **CatAg** catalyzing these reactions [40].



Scheme 1. Schematic of CatAg-catalyzed A3 coupling reactions. (I) Addition reaction between catalyst CatAg and PAE. (II) Hydrogen migration reaction involving an amine. (III) Amine aldehyde condensation reaction generates a molecule of water and an imine ion (Imine). (IV) Imine reacts with silver phenylacetylide (Ag_PAI), generating the A3 coupling reaction product PPA. (V) Cycloaddition reaction between the triple bond and $-N_3$ group in PPA generates the PR, and the catalyst CatAg is regenerated.

2. Results and Discussion

2.1. Addition Reaction between CatAg and PAE

Initially, we focused on the addition reaction between **CatAg** and **PAE**. Figure 1 illustrates the path of the addition reaction, and Figure 2 illustrates the molecular structures.

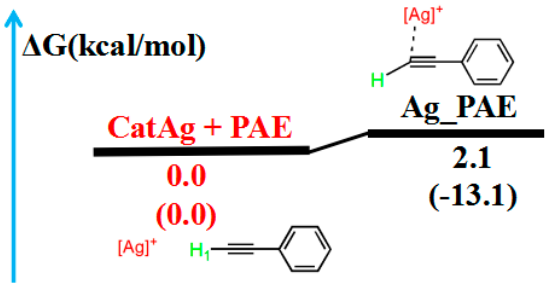


Figure 1. Reaction pathway of the addition reaction between catalyst CatAg and PAE. The relative free energy of the reaction pathway involving hydrogen is provided in kcal/mol. The relative enthalpy is also provided in brackets for reference (in kcal/mol).

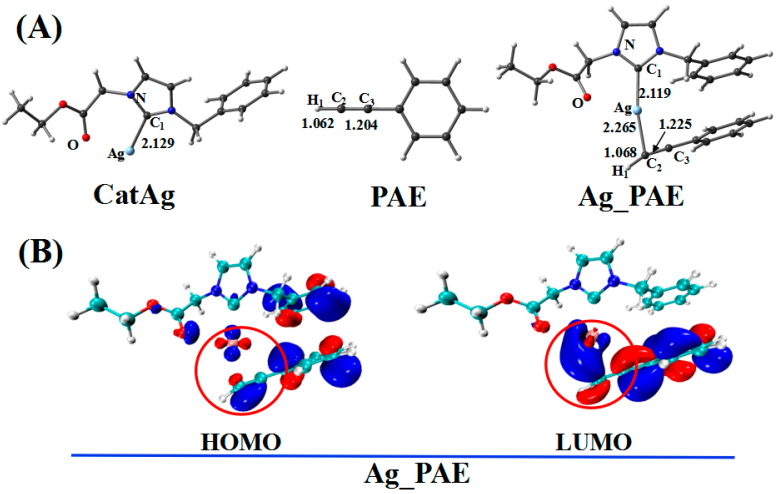


Figure 2. (**A**) Optimized geometries in addition reaction pathway between catalyst CatAg and PAE. Critical bond lengths are in Å. (**B**) Frontier orbitals of Ag_PAE.

In the addition reaction, the C_2 atom of PAE bonds to the center metal, Ag, of the catalyst CatAg, forming the product Ag_PAE. Because of coordination in the structure of the product Ag_PAE, C_2–H_1 (1.068 Å) and C_2–C_3 (1.225 Å) bonds are longer than those (1.062 and 1.204 Å) in PAE; the Ag–C_1 (2.119 Å) bond is shorter than that (2.129 Å) in CatAg. The frontier molecular orbitals of product Ag_PAE also illustrate the apparent interaction between PAE and CatAg. Figure 2B shows the highest occupied molecular orbital (HOMO) and lowest unoccupied molecular orbital (LUMO) of Ag_PAE. The Ag d_{x2-y2} orbital interacts with the π orbitals of the triple bond in the HOMO. Meanwhile, the Ag *s* orbitals appropriately combine with π anti-bonding orbitals of the C_2–C_3 triple bond in the LUMO.

Table 1 lists the Wiberg bond indices (WBIs) and natural bond orbital (NBO) charges (natural charges) for the addition reaction between CatAg and PAE. WBIs of the C_2–H_1 (from 0.934 to 0.899) and C_2–C_3 (from 2.825 to 2.623) bonds in the product Ag_PAE gradually decreased compared with those in the reactant (CatAg + PAE), indicating the weakening of the C_2–H_1 and C_2–C_3 bonds. Furthermore, Q_{NBO} value of the C_2 atom in the product (−0.187 e) was higher than that in the reactant PAE (−0.201 e). Meanwhile, the WBIs of the Ag–C_1 (from 0.482 to 0.491) and Ag–C_2 (from 0.000 to 0.199) bonds in the product Ag_PAE increased compared with those in the reactant (CatAg + PAE), indicating the strengthening of the Ag–C_1 and Ag–C_2 bonds. The energy of the product Ag_PAE is slightly higher than that of the reactant (CatAg + PAE) by a value of 2.1 kcal/mol, indicating that the experiment is easy to perform.

Table 1. The Wiberg bond indices (WBIs) and natural charges (Q_{NBO}) for the addition reaction between catalyst CatAg and PAE.

	WBI				Q_{NBO} (e)	
	B (C_2–H_1)	**B (C_2–C_3)**	**B (Ag–C_1)**	**B (Ag–C_2)**	**C_2**	**Ag**
CatAg + PAE	0.934	2.825	0.482	0.000	−0.201	0.701
Ag_PAE	0.899	2.623	0.491	0.199	−0.187	0.469

2.2. Hydrogen Migration Reaction Involving Amine

After PAE bonds to CatAg, a hydrogen migration reaction involving the amine occurs through the reaction path presented in Figure 3. The corresponding molecular geometries are shown in Figure 4. The hydrogen migration reaction involving amines starts with TS1 and proceeds to the product (Ag_PAI + AmineH).

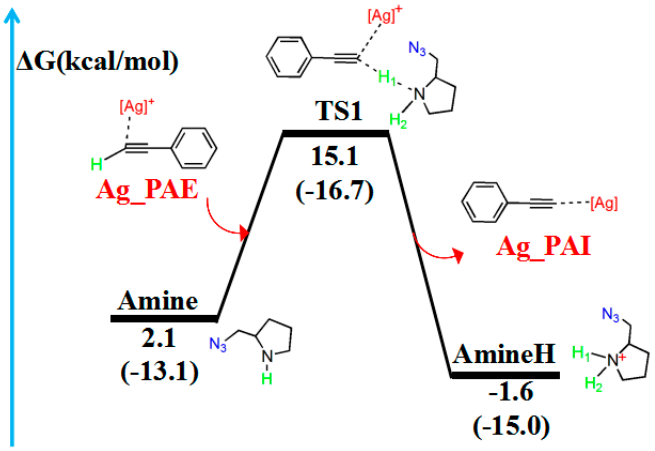


Figure 3. Reaction pathway of the hydrogen migration reaction involving amines. The relative free energy of the reaction pathway involving hydrogen is provided in kcal/mol. The relative enthalpy is also provided in brackets for reference (in kcal/mol).

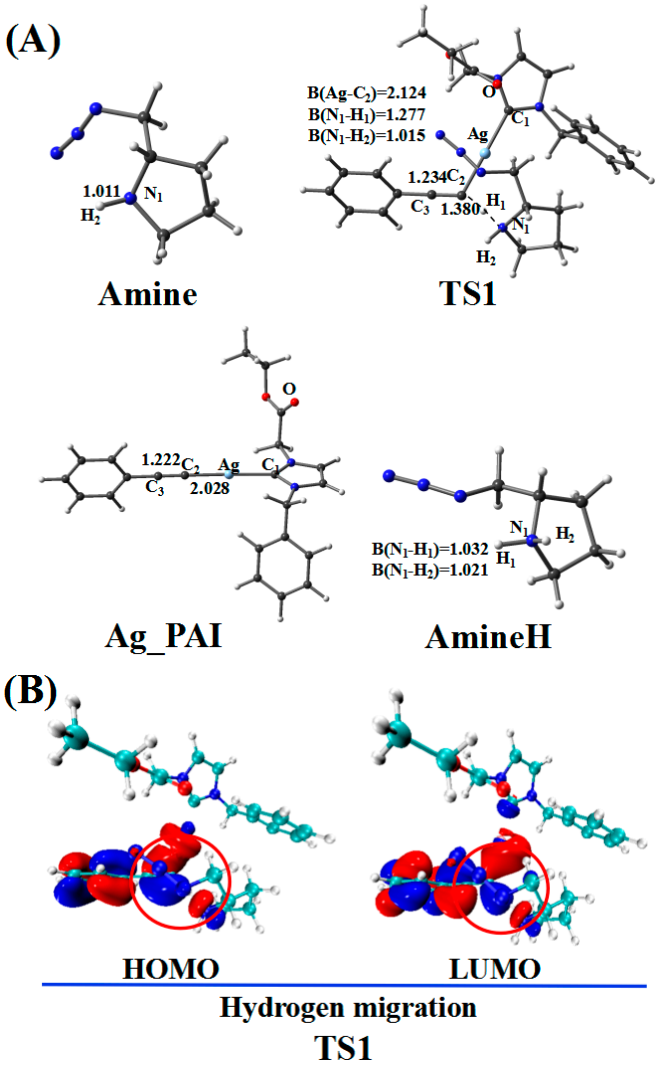


Figure 4. (**A**) Optimized geometries in the hydrogen migration pathway involving amines; the critical bond lengths are in Å. (**B**) Frontier orbitals of TS1.

In the reaction pathway, the H_1 atom of Ag_PAE first coordinated to the nitrogen atom (N_1) of the Amine, forming TS1. The bond length of C_2–H_1 (1.380 Å) and C_2–C_3 (1.234 Å) bonds in TS1 are longer than those in Ag_PAE (1.068 and 1.225 Å, respectively). TS1 has a unique imaginary frequency of –994.9 cm^{-1}, which shows the vibration characteristics of hydrogen migration between C_2 and N_1. The frontier orbitals of TS1 also show their respective hydrogen migration reaction characteristics.

After the formation of TS1, the C_2–H_1 bond breaks to form the product (Ag_PAI + AmineH). The hydrogen atom H_1 migrates from Ag_PAE to AmineH. Compared with those of the TS1 configuration, the C_2–C_3 (1.222 Å) and N_1–H_1 (1.032 Å) bonds of the product (Ag_PAI + AmineH) are shortened (1.234 and 1.277 Å) by 0.012 and 0.245 Å, respectively; the N_1–H_2 bond (1.021 Å) of AmineH is longer than that (1.015 Å) in the TS1 configuration by 0.006 Å.

Table 2 lists WBIs and NBO charges for the hydrogen migration reaction involving the amine. WBIs of the C_2–H_1 bond (from 0.899 to 0.000) in the product (Ag_PAI + AmineH) gradually decrease compared with those in the reactant (Ag_PAE + Amine), indicating the breakage of the C_2–H_1 bond. In contrast, WBIs of the N_1–H_1 bond (from 0.000 to 0.739) in the product (Ag_PAI + AmineH) increase compared with those in the reactant (Ag_PAE + Amine), indicating the N_1–H_1 bond is formed. Additionally, Q_{NBO} values of H_1 atom increase from 0.174 e in (Ag_PAE + Amine) to 0.458 e in (Ag_PAI + AmineH). Relative to the reactant (Ag_PAE + Amine), the energy barrier is 13.0 kcal/mol, and the reaction is exergonic, releasing 3.7 kcal/mol, revealing that it is feasible. The results are similar to those of a previous study in which alkyne deprotonation had a low transition state barrier when using gold catalysts [39].

Table 2. WBI and Q_{NBO} values for hydrogen migration reaction pathway involving amine.

	WBI				**Q_{NBO} (e)**		
	B (C_2–H_1)	**B (N_1–H_1)**	**B (C_2–C_3)**	**B (N_1–H_2)**	**H_1**	**N_1**	**H_2**
Ag_PAE + Amine	0.899	0.000	2.623	0.845	0.174	−0.703	0.362
TS1	0.464	0.347	2.617	0.810	0.362	−0.438	0.263
Ag_PAI + AmineH	0.000	0.739	2.759	0.792	0.458	−0.564	0.425

2.3. Amine–Aldehyde Condensation Reaction

The amine–aldehyde condensation reaction generates a water molecule and an imine ion [41,42]. The amine–aldehyde condensation reaction can procced via two pathways: with (Path one) or without (Path two) another amine catalyst. Figures 5 and 6 illustrate the reaction path of the amine–aldehyde condensation reaction and the molecular structures, respectively.

In the amine–aldehyde condensation reaction, one hydrogen atom (H_1) of AmineH first coordinates to the oxygen (O_1) atom of the aldehyde (Ald) to form the intermediate IM1. Compared with the reactant (AmineH + Ald), because of coordination, C_4–O_1 (1.222 Å) and N_1–H_1 (1.044 Å) bonds in IM1 are lengthened by 0.018 and 0.012 Å, respectively. Subsequently, TS2 is formed, and the H_1 atom migrates from N_1 to O_1. TS2 has a unique imaginary frequency of –138.3 cm^{-1}, which shows the vibration characteristics of the H_1 atom migration between N_1 and O_1. The N_1–H_1 (2.546 Å) and C_4–O_1 (1.272 Å) bonds are longer than those of IM1 (1.044 and 1.222 Å, respectively), whereas the O_1–H_1 bond (0.978 Å) is shorter than that (1.723 Å) in IM1. Relative to that of the reactant (AmineH + Ald), the energy potential barrier of TS2 is 27.9 kcal/mol. Compared with those in TS2, the C_4–N_1 (1.524 Å) and O_1–H_1 (0.963 Å) bonds in IM2 are shorter; however, the C_4–O_1 (1.403 Å) bond is longer.

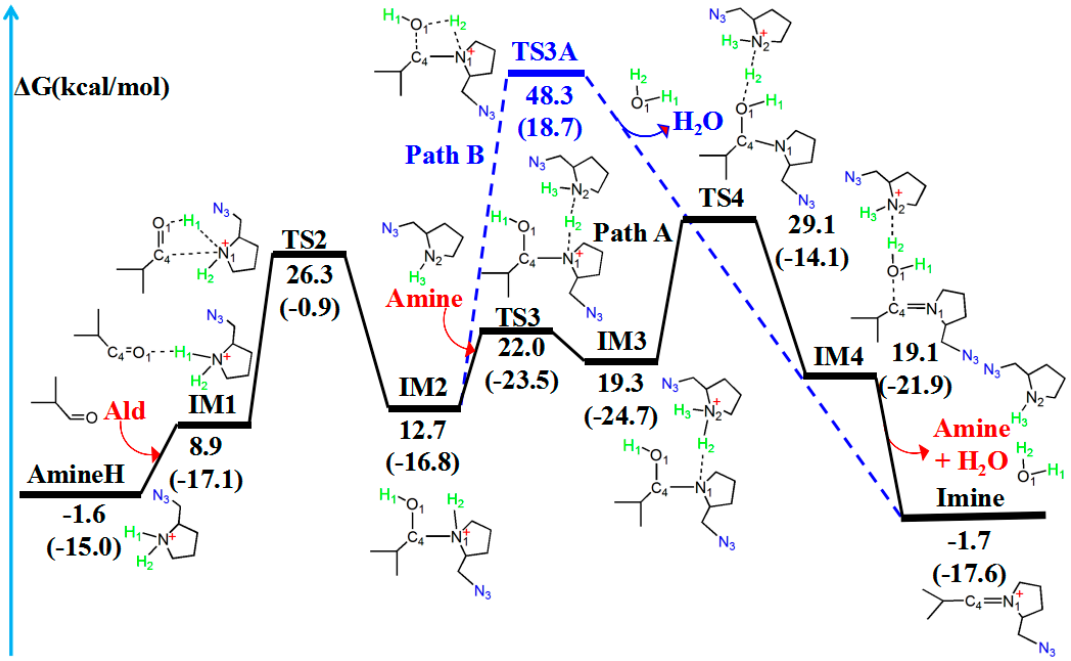


Figure 5. Amine–aldehyde condensation reaction pathway with (Path 1, in black) or without (Path 2, in blue) another amine catalyst. The relative free energy of the reaction pathway involving hydrogen is provided in kcal/mol. The relative enthalpy is also provided in brackets for reference (in kcal/mol).

After the formation of the intermediate IM2, the reaction can proceed via two pathways: with (Path one) or without (Path two) another amine catalyst. In Path one, with another amine catalyst, the H_2 hydrogen atom of IM2 coordinates to the N_2 nitrogen atom of another amine, forming TS3. TS3 has a unique imaginary frequency of –865.2 cm^{-1}, which shows the vibration characteristics of the H_2 atom migration between N_1 and N_2. The N_1–H_2 bond (1.300 Å) in TS3 is longer than that of IM2 (1.023 Å), whereas the C_4–N_1 bond length decreases from 1.524 Å in IM2 to 1.490 Å in TS3. Thereafter, the formation of IM3 occurs. The N_1–H_2 bond (1.740 Å) in the IM3 configuration is longer than that (1.300 Å) in the TS3, whereas the N_2–H_2 bond (1.075 Å) is shorter. The H_2 atom then migrates from N_1 to N_2. After the formation of IM3, TS4 is formed. TS4 has a unique imaginary frequency of –610.8 cm^{-1}, which shows the vibration characteristics of the H_2 atom migration between N_2 and O_1. The N_2–H_2 (1.202 Å) and C_4–O_1 (1.954 Å) bonds increase in length. Thereafter, the N_2–H_2 bond is further lengthened to 1.805 Å, and another intermediate IM4 is formed. The H_2 atom migrates from N_2 to O_1. Afterward, the N_2–H_2 and C_4–O_1 bonds break, leading to the formation of the product (Imine + H_2O).

Table 3 lists WBI and Q_{NBO} values for the amine–aldehyde condensation reaction. As the reaction proceeds from the reactant (AmineH + Ald) to form the product (Imine + H_2O), N_1–H_1 and C_4–O_1 WBIs decrease from 0.739 to 0.009 and from 1.886 to 0.002, respectively, implying the breakage of these bonds. However, WBIs of the O_1–H_1 (from 0.071 to 0.813) and O_1–H_2 (from 0.004 to 0.813) bonds gradually increase, indicating the formation of free H_2O. Relative to the reactant (AmineH + Ald), the energy barrier of Path one is 30.7 kcal/mol and the energy of the product (Imine + H_2O) is similar.

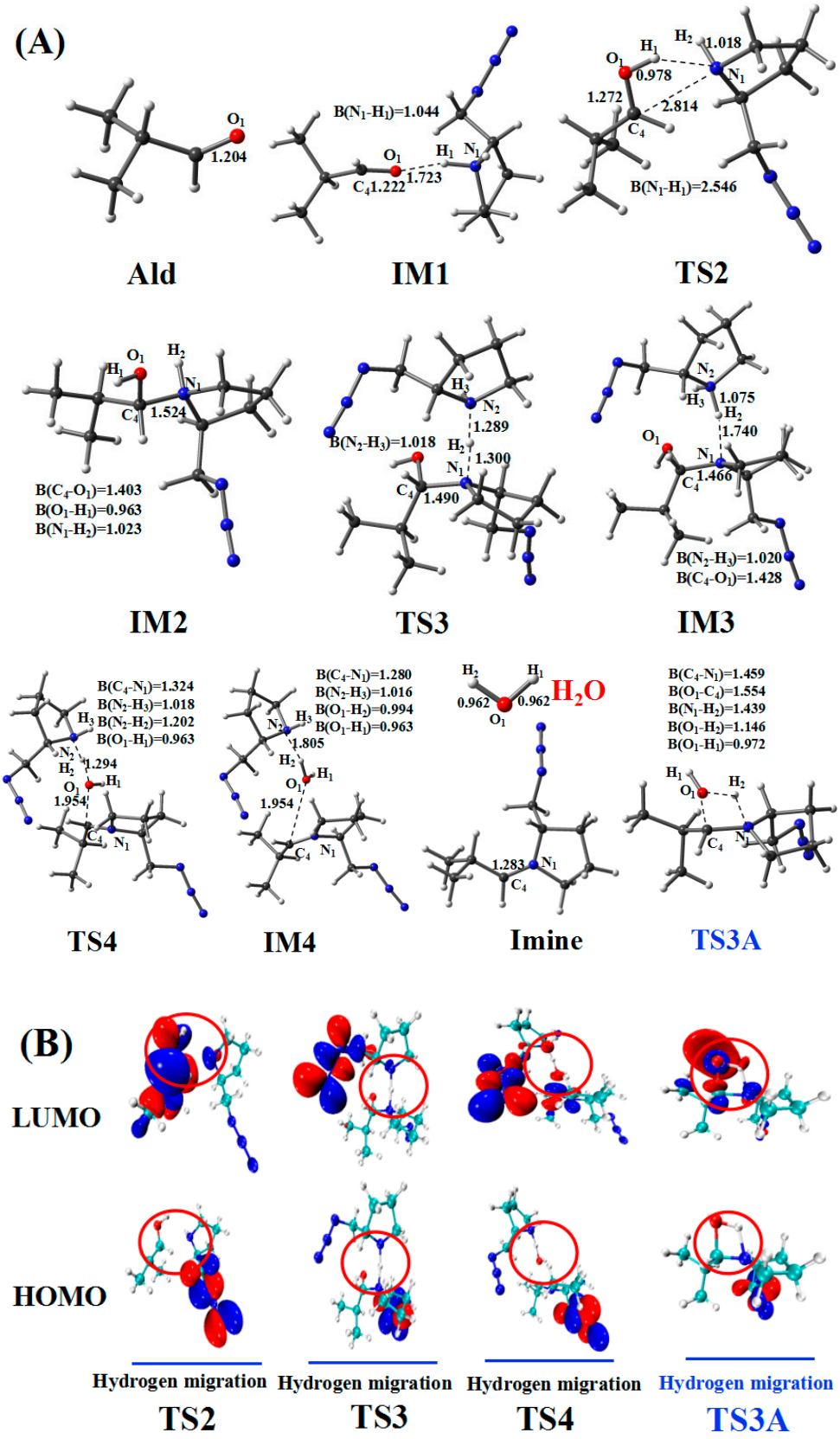


Figure 6. (**A**) Optimized geometries for the amine–aldehyde condensation reaction pathway; the critical bond lengths are in Å. (**B**) Frontier orbitals of TS2, TS3, TS4, and TS3A.

Table 3. WBI and Q_{NBO} values for the amine–aldehyde condensation reaction.

	WBI				Q_{NBO} (e)		
	B (N_1–H_1)	**B (C_4–O_1)**	**B (O_1–H_1)**	**B (O_1–H_2)**	**O_1**	**H_1**	**H_2**
AmineH + Ald	0.739	1.886			−0.515	0.458	0.425
IM1	0.693	1.734	0.071		−0.639	0.459	0.423
TS2	0.008	1.405	0.697		−0.526	0.521	0.360
IM2	0.009	0.950	0.745		−0.740	0.491	0.417
TS3		0.917	0.750	0.004	−0.766	0.482	0.484
IM3		0.893	0.756	0.004	−0.785	0.478	0.485
TS4		0.636	0.783	0.299	−0.963	0.463	0.471
IM4		0.002	0.795	0.670	−0.984	0.456	0.493
Imine + H_2O			0.813	0.813	−0.877	0.438	0.438
TS3A		0.790	0.674	0.411	−0.695	0.526	0.524

Path two for the amine–aldehyde condensation reaction starts from IM2. In contrast to Path one, which requires another amine catalyst, Path two directly yields the same product through a four-membered cyclic hydrogen migration transition state (TS3A). TS3A has a unique imaginary frequency of –1431.2 cm^{-1}, which shows the vibration characteristics of the H_2 atom migration between N_1 and O_1. Relative to the reactant (AmineH + Ald), the energy barrier of Path two was 49.9 kcal/mol. This value is very high compared to that of Path one (30.7 kcal/mol), and, therefore, Path two is not the dominant pathway.

2.4. Imine Reaction with Ag_PAI

Imine reacted with Ag_PAI to generate the A3 coupling reaction product PPA. Figures 7 and 8 illustrate the reaction path of Imine with Ag_PAI and the molecular structures, respectively.

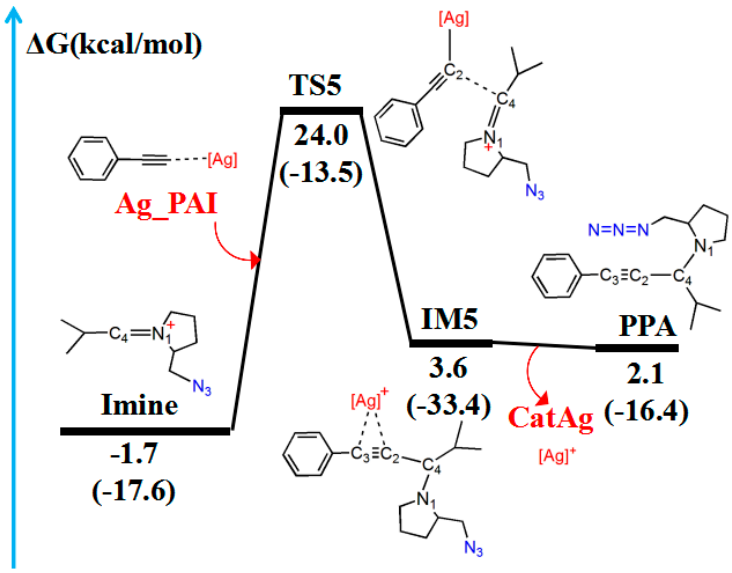


Figure 7. Reaction pathway of Imine and Ag_PAI. The relative free energy of the reaction pathway involving hydrogen is provided in kcal/mol. The relative enthalpy is also provided in brackets for reference (in kcal/mol).

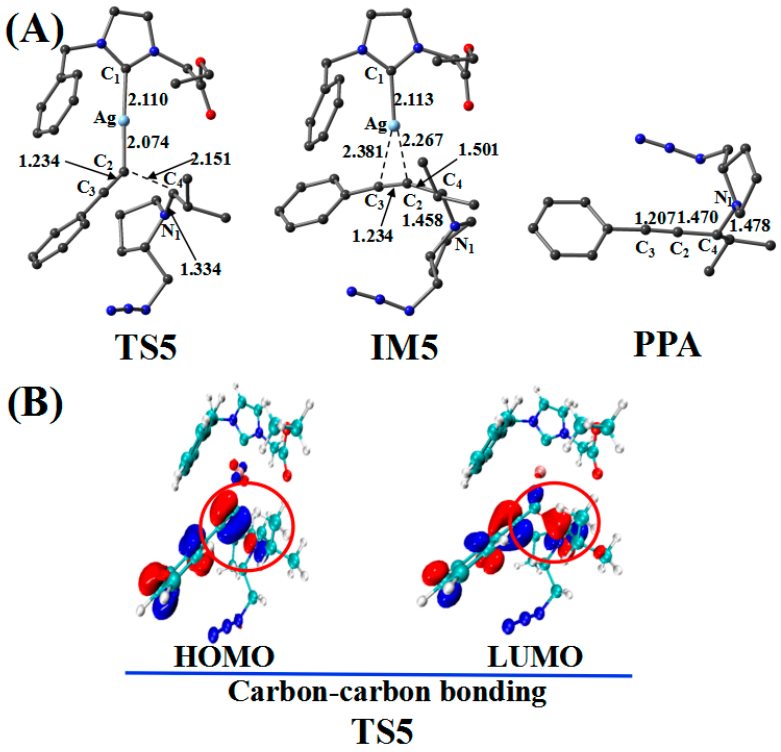


Figure 8. (**A**) Optimized geometries in the reaction pathway of Imine and Ag_PAI; the critical bond length is in Å. Hydrogen atom has been omitted for clarity. (**B**) Frontier orbitals of TS5.

The reaction first forms a carbon–carbon (C_2–C_4) bonding transition state (TS5). The Ag–C_2 (2.074 Å), C_2–C_3 (1.234 Å), and C_4–N_1 (1.334 Å) bonds in the TS5 configuration are longer than those (2.028, 1.222, and 1.283 Å, respectively) in the reactant (Ag_PAI + Imine). TS5 has a unique imaginary frequency of –134.8 cm^{-1}, which shows the vibration characteristics of carbon(C_2)–carbon(C_4) bonding. The frontier molecular orbitals of TS5 showed their respective carbon–carbon bonding reaction characteristics (Figure 8B). The C_2 p_x orbital appropriately combined with the C_4 p_y orbital of the LUMO. The formation of IM5 subsequently occurred. The C_2–C_4 bond length decreased from 2.151 Å in TS5 to 1.501 Å in IM5. Thereafter, the Ag–C_2 and Ag–C_3 bonds break, releasing the catalyst components CatAg and PPA. The C_2–C_4 (1.470 Å) and C_2–C_3 (1.207 Å) bonds in the PPA configuration are shorter than those in IM5, whereas the C_4–N_1 (1.478 Å) bond is longer.

Table 4 lists WBI and Q_{NBO} values for the imine ion and the silver phenylacetylide (Ag_PAI) reaction. As the reaction proceeds, from the reactant (Ag_PAI + Imine) to form the product (CatAg + PPA), the Ag–C_2 bond gradually elongates until its breakage (WBI decreases from 0.627 to 0.000). The C_4–N_1 bond gradually elongates until it changes from a double bond to a single bond (WBI decreases from 1.669 to 0.946), and the C_2–C_4 bond shortens until a stable bond is formed (WBI increases from 0.000 to 1.034). Relative to the reactant (Ag_PAI + Imine), the energy barrier is 25.7 kcal/mol and the energy of the product (CatAg + PPA) is slightly higher (3.8 kcal/mol).

Table 4. WBI and Q_{NBO} values for the imine ion and the silver phenylacetylide (**Ag_PAI**) reaction.

	WBI			**Q_{NBO} (e)**		
	B (Ag–C_2)	**B (C_4–N_1)**	**B (C_2–C_4)**	**C_2**	**N_1**	**C_4**
Ag_PAI + Imine	0.627	1.669	0.000	−0.386	−0.313	0.316
TS5	0.399	1.332	0.378	−0.449	−0.412	0.223
IM5	0.162	0.974	0.991	−0.097	−0.513	−0.062
CatAg + PPA	0.000	0.946	1.034	−0.386	−0.534	−0.082

2.5. Cycloaddition Reaction

The triple bond and N_3 group in PPA can undergo cycloaddition reactions [43] to generate the PR. Figures 9 and 10 illustrate the path of the cycloaddition reaction and the molecular structures, respectively.

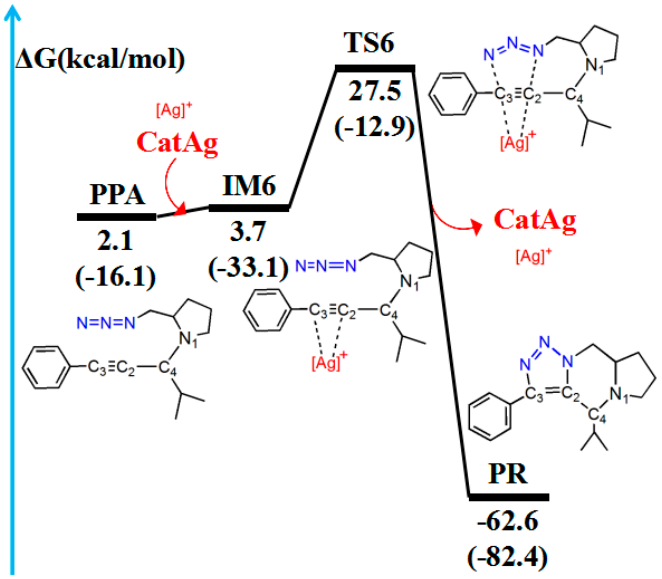


Figure 9. Pathway for the cycloaddition reaction between the triple bond and the $-N_3$ group in PPA. The relative free energy of the reaction pathway involving hydrogen is provided in kcal/mol. The relative enthalpy is also provided in brackets for reference (in kcal/mol).

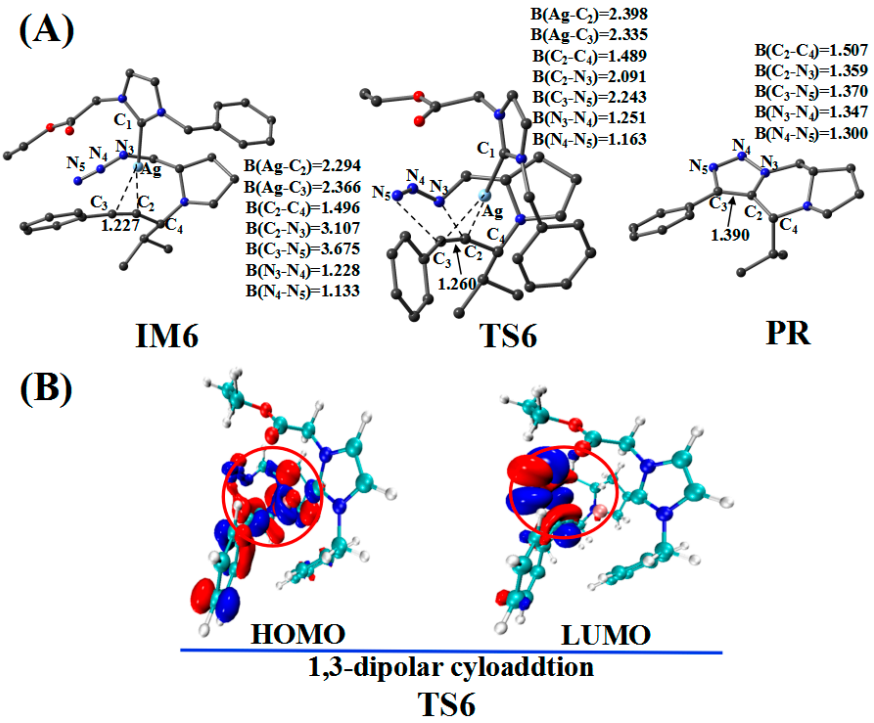


Figure 10. (**A**) Optimized geometries for the cycloaddition reaction; the critical bond length is in Å. Hydrogen atom has been omitted for clarity. (**B**) Frontier orbitals of TS6.

The CatAg first re-coordinates with the C_2–C_3 bond of PPA and forms the intermediate IM6. Because of the coordination, the C_2–C_3 bond (1.227 Å) in IM6 is longer than that (1.207 Å) in PPA by 0.020 Å. Immediately after the formation of IM6, the five-member

cycloaddition occurs and forms TS6. TS6 has a unique imaginary frequency of –423.7 cm^{-1}, which shows the vibration characteristics of a cycloaddition reaction. The frontier orbitals of TS6 exhibit their respective cycloaddition reaction characteristics (Figure 10B). Figure 10B shows the HOMO and LUMO orbitals of TS6. The C_2–C_3 bond π orbital interacts with the π orbital of the $-N_3$ group in HOMO. Meanwhile, the C_2–C_3 bond π orbital combines with the π anti-bonding orbital of the $-N_3$ group in LUMO. In the TS6 configuration, the C_2–N_3 (2.091 Å) and C_3–N_5 (2.243 Å) bonds are significantly shorter than those in IM6 (3.107 and 3.675 Å). Next, TS6 releases CatAg, thereby forming PR. Significantly, the C_2–N_3 (1.359 Å) and C_3–N_5 (1.370 Å) bonds in the PR are further shortened.

Table 5 lists WBI and Q_{NBO} values for the cycloaddition reaction. In the pathway of cycloaddition reaction, when the reaction proceeds from the reactant (PPA) to the PR, the C_2–C_3 bond gradually elongates until it changes from a triple bond to a double bond (WBI decreases from 2.716 to 1.420), and the C_2–N_3 (WBI increases from 0.002 to 1.206) and C_3–N_5 (WBI increases from 0.001 to 1.310) bonds shorten until stable bonds are formed. Compared with the reactant (PPA), the energy barrier is 25.4 kcal/mol, and the reaction is exergonic, releasing 64.7 kcal/mol. Therefore, the reaction is easy to conduct, which is similar to the experimental results [40].

Table 5. WBI and Q_{NBO} values for cycloaddition reaction.

	WBI					**Q_{NBO} (e)**	
	B (C_2–C_3)	**B (C_2–N_3)**	**B (C_3–N_5)**	**B (N_3–N_4)**	**B (N_4–N_5)**	**C_2**	**C_3**
CatAg + PPA	2.716	0.002	0.001	1.529	2.315	−0.002	−0.028
IM6	2.550	0.004	0.003	1.504	2.334	−0.084	−0.013
TS6	2.249	0.316	0.285	1.455	2.144	−0.021	−0.105
PR + CatAg	1.420	1.206	1.310	1.221	1.537	0.140	0.075

To further study these reactions, conceptual density functional theory (CDFT) calculations were performed (Table 6). The global reactivity index (GRI) values reveal the nucleophilicity and electrophilicity of the molecules. The global nucleophilicity (N_{Nu}) values of PAE, PPA, and Ag_PAI are 2.825, 3.216, and 4.215, respectively, which indicate the nucleophilicities of these molecules. Meanwhile, the global electrophilicity (ω) values of CatAg and Imine are 3.795 and 4.172, respectively, which indicate that they are electrophilic.

Table 6. GRI and Fukui function data for certain molecules.

	η [a]	μ [b]	ω [c]	N_{Nu} [d]	f^{+} [e]		f^{-} [f]
					Ag	**C_4**	**C_2**
CatAg	7.424	−7.623	3.795	−0.330	0.693		
PAE	9.577	−3.561	0.839	2.825			0.197
PPA	8.347	−3.278	0.847	3.216			0.064
Imine	8.598	−8.503	4.172	−1.172		0.212	
Ag_PAI	7.073	−3.077	0.818	4.215			0.172

[a] Chemical hardness (η, eV). [b] Electronic chemical potential (μ, eV). [c] Global electrophilicity (ω, eV). [d] Global nucleophilicity (N_{Nu}, eV). [e] Nucleophilic attack Fukui function for Ag, C_4 (f^{+}, e). [f] Electrophilic attack Fukui function for C_2 (f^{-}, e).

Table 6 and Figure 11 present the Fukui function data for certain molecules. The data illustrate that the Fukui function values (f^{+}) of Ag (0.693) and C_4 (0.212) atoms are the most significant parameters for CatAg and Imine; therefore, Ag (CatAg) and C_4 (Imine) atoms have higher reactivity. At the same time, the Fukui function values (f^{-}) of C_2 in PAE (0.197), PPA (0.064), and Ag_PAI (0.172) are the highest. This indicates that the C_2 atoms have higher reactivity and can easily react with Ag (CatAg) and C_4 (Imine) atoms to complete the reactions. This result is similar to the experimental results [40].

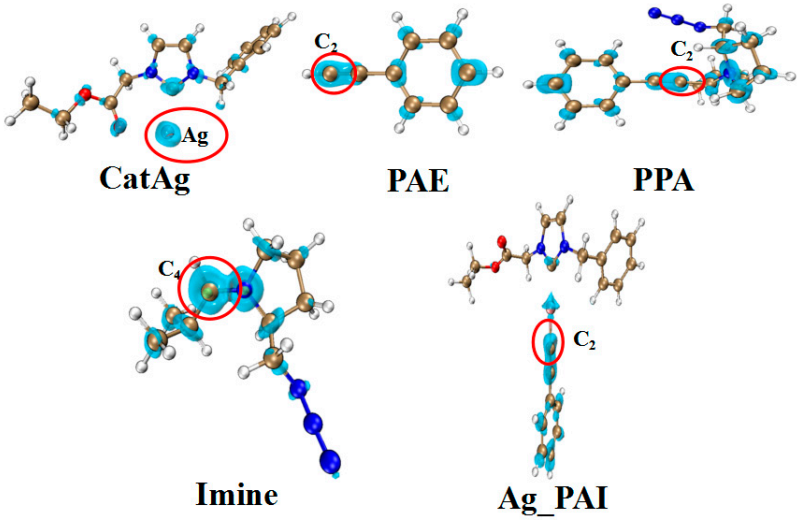


Figure 11. Isosurface diagram of the Fukui function for Ag (CatAg, f^+), C_4 (Imine, f^+), and C_2 (f^-) in PAE, PPA, and Ag_PAI.

In order to better understand the intrinsic characteristics of the reaction and to understand the influence of the concentration of the catalyst (**CatAg**) on the reaction, the concvar program [44] was used. This program simulates the change in the concentration of various substances over the reaction time of the study and provides kinetic data based on the calculated reaction profile. Note that in order to facilitate the study, the reaction pathway was appropriately simplified, and some low-barrier transition states and insignificant intermediates in the reaction path were ignored. The initial concentrations of each of the three reactants (PAE, Amine, and Ald) for this simulation were set to 1.0 M and the catalyst concentration was set to 0.02 M at 333.15 K for 500,000 s. The concentration changes in each substance throughout the simulation process are shown in Figure 12.

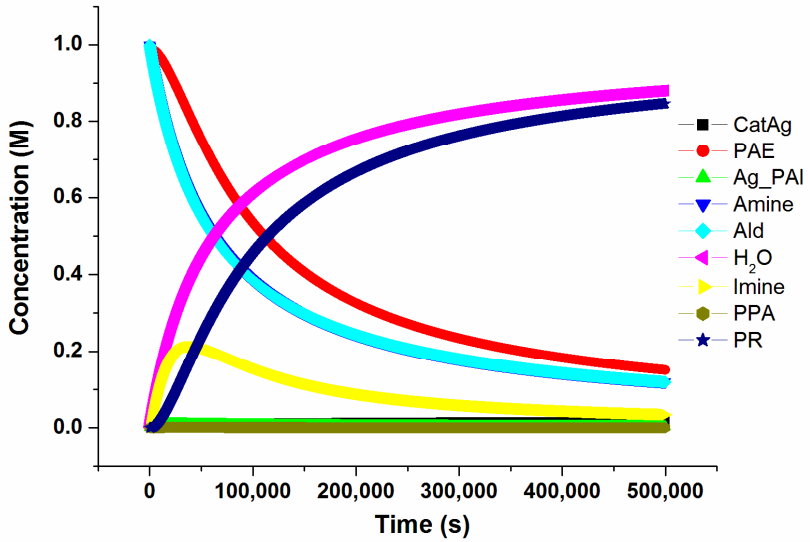


Figure 12. The change in the concentration of various substances over reaction time.

Figure 12 shows that the three reactants (PAE, Amine, and Ald) are consumed at approximately the same rate; hence, it is reasonable to consider that the starting concentrations of the three reactants are nearly equal. This is consistent with the experimental results. At the beginning of the reaction, the concentration of Imine increases first and then decreases gradually as the reaction progresses and the product is formed. The concentration of PPA

remains low because PPA reacts easily and forms PR. The concentrations of the product (PR) and H_2O increase rapidly at the beginning and then more slowly as the reaction progresses.

The yield of the product (PR) varies with the catalyst (CatAg) concentration at a constant reaction time of 500,000 s, as shown in Figure 13. The yield of the product (PR) increases with increasing catalyst (CatAg) concentration. In particular, the product (PR) yield increases rapidly when the catalyst (CatAg) concentration increases from 0.00 M to 0.02 M. After 0.02 M, the product (PR) yield increases slowly with increasing catalyst (CatAg) concentration.

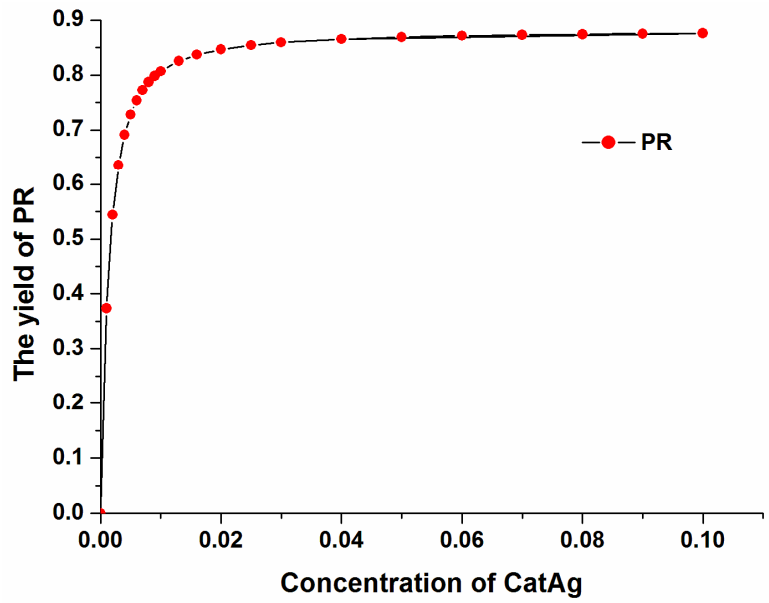


Figure 13. The yield of product (PR) varies with the catalyst (CatAg) concentration.

3. Computational Methods

All computations were performed using the DFT method employing the Gaussian 16 program [45]. All structures were optimized and characterized by frequency analysis calculations to be minima (without imaginary frequencies) or transition states (TSs) (having unique imaginary frequencies) at the *B3LYP-D3*(BJ)/BS level [46–49]. BS, as a basis set, unites the SDD [50] for Ag and 6-311G (d,p) for nonmetal atoms. A pseudopotential base set was adopted for Ag atoms. The intrinsic reaction coordinate (IRC) [51] approach was used to identify the transition states connecting the reactants with the products. The thermodynamic corrections (the correction factor is 0.9670) were calculated based on a rigid-rotor harmonic oscillator (RRHO) model using the Shermo program under 333.15 K and 1 atm [52]. To improve the energetic results, single-point energy calculations for the optimized structures were performed at the M06-2X/def2-TZVP level [53,54] using the SMD [55] solvent effects model. Free energies obtained using M06-2X (SMD, solvent = acetonitrile)/def2TZVP were considered throughout this study; the relative enthalpies were also provided for reference. The WBI and NBO charges [56] were calculated at the *B3LYP-D3*(BJ)/BS level. Houk and coworkers [57] recommended the M06-2X//B3LYP combination to study transition metal-catalyzed reactions. The protocol has been successfully applied to study the mechanisms of transition metal-catalyzed reactions [58–66].

Frontier orbitals and certain CDFT data, such as the GRI [67–70] and Fukui functions [71,72], were obtained using the Multiwfn program 3.8 [73]. The diagrams for the frontier orbitals and isosurface of the Fukui function were plotted using the VMD program 1.9.3 [74]. The change in the concentration of various substances over the reaction time was simulated using the concvar program [44], and the reaction rate constants were calculated based on the transition state theory [75]. Additional computational details and detailed data

of Fukui functions values for some molecules are given in Table S1. Energies, vibrational frequencies and Cartesian coordinates of all the optimized structures are given in Table S2.

4. Conclusions

The A3 coupling reactions catalyzed by CatAg were calculated using DFT. First, an addition reaction between CatAg and PAE forms Ag_PAE. Subsequently, one hydrogen atom of the Ag_PAE migrates to the nitrogen atom of the Amine. Thereafter, the amine–aldehyde condensation reaction generates a water molecule and an Imine. The amine–aldehyde condensation reaction can proceed through two pathways: with (Path one) or without (Path two) another amine catalyst. Path one has a lower reaction barrier than Path two. The Imine reacts with Ag_PAI to generate the A3 coupling reaction product, PPA. Moreover, the cycloaddition reaction between the triple bond and $-N_3$ group in PPA generates the PR, and the CatAg is regenerated. The entire reaction is strongly exothermic, and, therefore, it is easy to perform, which is consistent with our experimental results. Additionally, CDFT data analyses confirmed this reaction mechanism. The detailed mechanistic insights of these reactions presented in this paper advance the understanding of the reactions of aldehydes, alkynes, and amines catalyzed by CatAg and will be beneficial for developing a new synthesis strategy for similar functional compounds.

Supplementary Materials: The following supporting information can be downloaded at https://www.mdpi.com/article/10.3390/catal13040646/s1. Table S1: Additional computational details and detailed data of Fukui functions values for some molecules. Table S2: Energies, vibrational frequencies and Cartesian coordinates of all the optimized structures.

Author Contributions: Conceptualization, C.Z., S.Y. and J.C.; data curation, F.W. (Fei Wang), X.L., Y.Z., M.Y. and B.Z.; formal analysis, F.W. (Fuping Wang) and H.Z.; funding acquisition, C.Z., J.C. and F.W. (Fuping Wang); investigation, S.Y.; and project administration, C.Z. All authors have read and agreed to the published version of the manuscript.

Funding: This work was financially supported by the Science and Technology Project of Hebei Education Department (ZD2021090), the National Natural Science Foundation of China (22276134), the S&T Program of Hebei (B2020408007), the Science and Technology Research Projects of Langfang Normal University (XBQ202011), the Fundamental Research Funds for the Universities in Hebei Province (JYT202101), and the Innovation and Entrepreneurship Training Program of Langfang Normal University (X202210100016).

Data Availability Statement: The data presented in this study are available in the Supplementary Materials.

Conflicts of Interest: The authors declare no conflict of interest.

References

1. Qiu, S.; Chen, W.; Li, D.; Chen, Y.; Niu, Y.; Wu, Y.; Lei, Y.; Wu, L.; He, W. The use of propargylamines to synthesize amino-1,2,3-triazoles via cycloaddition of azides with allenamines. *Synthesis* **2022**, *54*, 2175–2184.
2. Jesin, I.; Nandi, G.C. Recent advances in the A3 coupling reactions and their applications. *Eur. J. Org. Chem.* **2019**, *16*, 2704–2720. [CrossRef]
3. Ermolat'ev, D.S.; Bariwal, J.B.; Steenackers, H.P.L.; De Keersmaecker, S.C.J.; Van der Eycken, E.V. Concise and diversity-oriented route toward polysubstituted 2-aminoimidazole alkaloids and their analogues. *Angew. Chem. Int. Ed.* **2010**, *49*, 9465–9468. [CrossRef]
4. Ganem, B. Strategies for innovation in multicomponent reaction design. *Acc. Chem. Res.* **2009**, *42*, 463–472. [CrossRef] [PubMed]
5. Zorba, L.P.; Vougioukalakis, G.C. The ketone-amine-alkyne (KA2) coupling reaction: Transition metal-catalyzed synthesis of quaternary propargylamines. *Coord. Chem. Rev.* **2021**, *429*, 213603. [CrossRef]
6. Ramazani, A.; Ahankar, H.; Nafeh, T.Z.; Joo, W.S. Modern catalysts in A_3—coupling reactions. *Curr. Org. Chem.* **2019**, *23*, 2783–2801. [CrossRef]
7. McNally, J.J.; Youngman, M.A.; Dax, S.L. Mannich reactions of resin-bound substrates: 2. A versatile three-component solid-phase organic synthesis methodology. *Tetrahedron Lett.* **1998**, *39*, 967–970. [CrossRef]
8. Dyatkin, A.B.; Rivero, R.A. The solid phase synthesis of complex propargylamines using the combination of sonogashira and mannich reactions. *Tetrahedron Lett.* **1998**, *39*, 3647–3650. [CrossRef]

9. Li, C.-J.; Wei, C. Highly efficient grignard-type imine additions via C-H activation in water and under solvent-free conditions. *Chem. Comm.* **2002**, *3*, 268–269. [CrossRef]
10. Shi, L.; Tu, Y.-Q.; Wang, M.; Zhang, F.-M.; Fan, C.-A. Microwave-promoted three-component coupling of aldehyde, alkyne, and amine via C-H activation catalyzed by copper in water. *Org. Lett.* **2004**, *6*, 1001–1003. [CrossRef]
11. Yadav, J.S.; Subba Reddy, B.V.; Naveenkumar, V.; Srinivasa Rao, R.; Nagaiah, K. [bmim]PF_6/CuBr: A novel and recyclable catalytic system for the synthesis of propargyl amines. *New J. Chem.* **2004**, *28*, 335–337. [CrossRef]
12. Bariwal, J.; Ermolat'ev, D.; Van der Eycken, E.V. Efficient microwave-assisted synthesis of secondary alkylpropargylamines by using A3-coupling with primary aliphatic amines. *Chem. Eur. J.* **2010**, *16*, 3281–3284. [CrossRef] [PubMed]
13. Kumar, A.; Kumar, M.; Maurya, S.; Khanna, R.S. Regioselective synthesis of fused imidazo[1,2-a]pyrimidines via intramolecular C-N bond formation/6-endo-dig cycloisomerization. *J. Org. Chem.* **2014**, *79*, 6905–6912. [CrossRef]
14. Bisai, V.; Suneja, A.; Singh, V.K. Asymmetric alkynylation/lactamization cascade: An expeditious entry to enantiomerically enriched isoindolinones. *Angew. Chem. Int. Ed.* **2014**, *53*, 10737–10741. [CrossRef]
15. Trose, M.; Dell'Acqua, M.; Pedrazzini, T.; Pirovano, V.; Gallo, E.; Rossi, E.; Caselli, A.; Abbiati, G. [Silver(I)(pyridine-containing ligand)] complexes as unusual catalysts for A3-coupling reactions. *J. Org. Chem.* **2014**, *79*, 7311–7320. [CrossRef] [PubMed]
16. Prakash, O.; Joshi, H.; Kumar, U.; Sharma, A.K.; Singh, A.K. Acridine based (S,N,S) pincer ligand: Designing silver(I) complexes for the efficient activation of A3 (aldehyde, alkyne and amine) coupling. *Dalton Trans.* **2015**, *44*, 1962–1968. [CrossRef] [PubMed]
17. Wang, Z.; Tzouras, N.V.; Nolan, S.P.; Bi, X. Silver N-heterocyclic carbenes: Emerging powerful catalysts. *Trends Chem.* **2021**, *3*, 674–685. [CrossRef]
18. Ghasemi, K.; Darroudi, M.; Rahimi, M.; Rouh, H.; Gupta, A.R.; Cheng, C.; Amini, A. Magnetic AgNPs/Fe_3O_4@chitosan/PVA nanocatalyst for fast one-pot green synthesis of propargylamine and triazole derivatives. *New J. Chem.* **2021**, *45*, 16119–16130. [CrossRef]
19. Xin, N.; Jing, X.; Zhang, C.-G.; Peng, X.; Liu, J.; Wang, Q.; Wang, W.; Cao, J.; Tao, M. N-heterocyclic carbene silver complex modified polyacrylonitrile fiber/MIL-101(Cr) composite as efficient chiral catalyst for three-component coupling reaction. *Nanomaterials* **2022**, *12*, 4175. [CrossRef]
20. Cao, J.; Li, P.; Xu, G.; Tao, M.; Ma, N.; Zhang, W. Cooperative N-heterocyclic carbene Au and amino catalysis for continuous synthesis of secondary propargylamines in a fiber supported hydrophilic microenvironment. *Chem. Eng. J.* **2018**, *349*, 456–465. [CrossRef]
21. Srinivas, V.; Koketsu, M. Synthesis of indole-2-, 3-, or 5-substituted propargylamines via gold(III)-catalyzed three component reaction of aldehyde, alkyne, and amine in aqueous medium. *Tetrahedron* **2013**, *69*, 8025–8033. [CrossRef]
22. Huang, J.-L.; Gray, D.G.; Li, C.-J. A3-coupling catalyzed by robust Au nanoparticles covalently bonded to HS-functionalized cellulose nanocrystalline films. *Beilstein J. Org. Chem.* **2013**, *9*, 1388–1396. [CrossRef] [PubMed]
23. Chen, H.-B.; Zhao, Y.; Liao, Y. Aldehyde-alkyne-amine (A3) coupling catalyzed by a highly efficient dicopper complex. *RSC Adv.* **2015**, *5*, 37737–37741. [CrossRef]
24. Trang, T.T.T.; Ermolat'ev, D.S.; Van der Eycken, E.V. Facile and diverse microwave-assisted synthesis of secondary propargylamines in water using CuCl/$CuCl_2$. *RSC Adv.* **2015**, *5*, 28921–28924. [CrossRef]
25. Neshat, A.; Gholinejad, M.; Afrasi, M.; Mastrorilli, P.; Todisco, S.; Gilanchi, S.; Osanlou, F. Heterocyclic thiolates and phosphine ligands in copper-catalyzed synthesis of propargylamines in water. *Appl. Organomet. Chem.* **2021**, *35*, e6180. [CrossRef]
26. Yadav, J.S.; Subba Reddy, B.V.; Hara Gopal, A.V.; Patil, K.S. $InBr_3$-catalyzed three-component reaction: A facile synthesis of propargyl amines. *Tetrahedron Lett.* **2009**, *50*, 3493–3496. [CrossRef]
27. Zhang, Y.; Li, P.; Wang, M.; Wang, L. Indium-catalyzed highly efficient three-component coupling of aldehyde, alkyne, and amine via C-H bond activation. *J. Org. Chem.* **2009**, *74*, 4364–4367. [CrossRef]
28. Li, P.; Zhang, Y.; Wang, L. Iron-catalyzed ligand-free three-component coupling reactions of aldehydes, terminal alkynes, and amines. *Chem. Eur. J.* **2009**, *15*, 2045–2049. [CrossRef]
29. Chen, W.-W.; Nguyen, R.V.; Li, C.-J. Iron-catalyzed three-component coupling of aldehyde, alkyne, and amine under neat conditions in air. *Tetrahedron Lett.* **2009**, *50*, 2895–2898. [CrossRef]
30. Huo, X.; Liu, J.; Wang, B.; Zhang, H.; Yang, Z.; She, X.; Xi, P. A one-step method to produce graphene-Fe3O4 composites and their excellent catalytic activities for three-component coupling of aldehyde, alkyne and amine. *J. Mater. Chem. A* **2013**, *1*, 651–656. [CrossRef]
31. Samai, S.; Nandi, G.C.; Singh, M.S. An efficient and facile one-pot synthesis of propargylamines by three-component coupling of aldehydes, amines, and alkynes via C-H activation catalyzed by $NiCl_2$. *Tetrahedron Lett.* **2010**, *51*, 5555–5558. [CrossRef]
32. Shi, X.-L.; Sun, B.; Chen, Y.; Hu, Q.; Li, P.; Meng, Y.; Duan, P. Tuning anion species and chain length of ligands grafted on the fiber for an efficient polymer-supported Ni(II) complex catalyst in one-pot multicomponent A3-coupling. *J. Catal.* **2019**, *372*, 321–329. [CrossRef]
33. Manikandan, R.; Anitha, P.; Viswanathamurthi, P.; Malecki, J.G. Palladium(II) pyridoxal thiosemicarbazone complexes as efficient and recyclable catalyst for the synthesis of propargylamines by a three-component coupling reactions in ionic liquids. *Polyhedron* **2016**, *119*, 300–306. [CrossRef]
34. Nouruzi, N.; Dinari, M.; Mokhtari, N.; Gholipour, B.; Rostamnia, S.; Khaksar, S.; Boluki, R. Porous triazine polymer: A novel catalyst for the three-component reaction. *Appl. Organomet. Chem.* **2020**, *34*, e5677. [CrossRef]

35. Li, J.; Xu, Y.; Hu, X.; Zhu, S.; Liu, L. Easy access to 2,4-disubstituted cyclopentenones by a gold(III)-catalyzed A3-coupling/cyclization cascade. *Org. Lett.* **2020**, *22*, 9478–9483. [CrossRef] [PubMed]
36. Xu, X.; Feng, H.; Van der Eycken, E.V. Microwave-assisted Cu(I)-catalyzed synthesis of unsymmetrical 1,4-diamino-2-butynes via cross-A3-coupling/decarboxylative A3-coupling. *J. Org. Chem.* **2021**, *86*, 14036–14043. [CrossRef]
37. Cao, S.; Zou, B.; Yang, J.; Wang, J.; Feng, H. Hollow CuO-CeO_2 nanospheres for an effectively catalytic annulation/A3-coupling reaction sequence. *ACS Appl. Nano Mater.* **2022**, *5*, 11689–11698. [CrossRef]
38. Kumar, G.; Pandey, S.; Gupta, R. Ag-based coordination polymers based on metalloligands and their catalytic performance in multicomponent A3-coupling reactions. *Cryst. Growth Des.* **2022**, *18*, 5501–5511. [CrossRef]
39. Costabile, C.; Mariconda, A.; Sirignano, M.; Crispini, A.; Scarpelli, F.; Longo, P. A green approach for A3-coupling reactions: An experimental and theoretical study on NHC silver and gold catalysts. *New J. Chem.* **2021**, *45*, 18509–18517. [CrossRef]
40. Cao, J.; Xu, G.; Li, P.; Tao, M.; Zhang, W. Polyacrylonitrile fiber supported N-heterocyclic carbene Ag(I) as efficient catalysts for three-component coupling and intramolecular 1,3-dipolar cycloaddition reactions under flow conditions. *ACS Sustain. Chem. Eng.* **2017**, *5*, 3438–3447. [CrossRef]
41. Li, Z.; Wang, Q.; Pu, M.; Yang, Z.; Lei, M. Theoretical study on nitrogenous heterocyclic assisted aldimine condensation. *Acta Chim. Sin.* **2020**, *78*, 437–443. [CrossRef]
42. Ciaccia, M.; Di Stefano, S. Mechanisms of imine exchange reactions in organic solvents. *Org. Biomol. Chem.* **2015**, *13*, 646–654. [CrossRef] [PubMed]
43. Boz, E.; Tüzün, N.Ş. Ag-catalyzed azide alkyne cycloaddition: A DFT approach. *Dalton Trans.* **2016**, *45*, 5752–5764. [CrossRef] [PubMed]
44. Lu, T. Concvar: A computer program for simulating concentration variation of complex chemical reactions. *ChemRxiv* **2022**, preprint. [CrossRef]
45. Frisch, M.J.; Trucks, G.W.; Schlegel, H.B.; Scuseria, G.E.; Robb, M.A.; Cheeseman, J.R.; Scalmani, G.; Barone, V.; Petersson, G.A.; Nakatsuji, H.; et al. *Gaussian 16, Revision C.01*; Gaussian, Inc.: Wallingford, CT, USA, 2016.
46. Becke, A.D. Density-functional thermochemistry. III. The role of exact exchange. *J. Chem. Phys.* **1993**, *98*, 5648–5652. [CrossRef]
47. Grimme, S.; Antony, J.; Ehrlich, S.; Krieg, H. A consistent and accurate Ab initio parametrization of density functional dispersion correction (DFT-D) for the 94 elements H-Pu. *J. Chem. Phys.* **2010**, *132*, 154104. [CrossRef]
48. Grimme, S.; Ehrlich, S.; Goerigk, L. Effect of the damping function in dispersion corrected density functional theory. *J. Comput. Chem.* **2011**, *32*, 1456–1465. [CrossRef]
49. Smith, D.G.; Burns, L.A.; Patkowski, K.; Sherrill, C.D. Revised damping parameters for the D3 dispersion correction to density functional theory. *J. Phys. Chem. Lett.* **2016**, *7*, 2197–2203. [CrossRef]
50. Miehlich, B.; Savin, A.; Stoll, H.; Preuss, H. Results obtained with the correlation energy density functionals of Becke and Lee, Yang and Parr. *Chem. Phys. Lett.* **1989**, *157*, 200–206. [CrossRef]
51. Fukui, K. The path of chemical reactions-the IRC approach. *Acc. Chem. Res.* **1981**, *14*, 363–368. [CrossRef]
52. Lu, T.; Chen, Q. Shermo: A general code for calculating molecular thermochemistry properties. *Comput. Theor. Chem.* **2021**, *1200*, 113249. [CrossRef]
53. Zhao, Y.; Truhlar, D.G. Density functionals with broad applicability in chemistry. *Acc. Chem. Res.* **2008**, *41*, 157–167. [CrossRef] [PubMed]
54. Zhao, Y.; Truhlar, D.G. Benchmark energetic data in a model system for grubbs II metathesis catalysis and their use for the development, assessment, and validation of electronic structure methods. *J. Chem. Theory Comput.* **2009**, *5*, 324–333. [CrossRef] [PubMed]
55. Marenich, A.V.; Cramer, C.J.; Truhlar, D.G. Universal solvation model based on solute electron density and on a continuum model of the solvent defined by the bulk dielectric constant and atomic surface tensions. *J. Phys. Chem. B* **2009**, *113*, 6378–6396. [CrossRef] [PubMed]
56. Reed, A.E.; Curtiss, L.A.; Weinhold, F. Intermolecular interactions from a natural bond orbital, donor-acceptor viewpoint. *Chem. Rev.* **1988**, *88*, 899–926. [CrossRef]
57. Yang, Y.-F.; Hong, X.; Yu, J.-Q.; Houk, K.N. Experimental–computational synergy for selective Pd(II)-catalyzed C–H activation of aryl and alkyl groups. *Acc. Chem. Res.* **2017**, *50*, 2853–2860. [CrossRef]
58. Deng, L.; Fu, Y.; Lee, S.Y.; Wang, C.; Liu, P.; Dong, G. Kinetic resolution via Rh-catalyzed C-C activation of cyclobutanones at room temperature. *J. Am. Chem. Soc.* **2019**, *141*, 16260–16265. [CrossRef]
59. Li, Y.; Chen, H.; Qu, L.-B.; Houk, K.N.; Lan, Y. Origin of regiochemical control in Rh(III)/Rh(V)-catalyzed reactions of unsaturated oximes and alkenes to form pyrdines. *ACS Catal.* **2019**, *9*, 7154–7165. [CrossRef]
60. Palani, V.; Hugelshofer, C.L.; Kevlishvili, I.; Liu, P.; Sarpong, R. A short synthesis of delavatine a unveils new insights into site-selective cross-coupling of 3,5-dibromo-2-pyrone. *J. Am. Chem. Soc.* **2019**, *141*, 2652–2660. [CrossRef]
61. Qi, X.; Kohler, D.G.; Hull, K.L.; Liu, P. Energy decomposition analyses reveal the origins of catalyst and nucleophile effects on regioselectivity in nucleopalladation of alkenes. *J. Am. Chem. Soc.* **2019**, *141*, 11892–11904. [CrossRef]
62. Zhang, C.; Yu, S.; Wang, F.; Wang, F.; Cao, J.; Zheng, H.; Chen, X.; Ren, A. Density functional theory analysis of the copolymerization of cyclopropenone with ethylene using a palladium catalyst. *Polymers* **2022**, *14*, 5273. [CrossRef]
63. Liu, Z.; Lu, Y.; Guo, J.; Hu, W.; Wang, Z.X. DFT mechanistic account for the site selectivity of electron-rich C(sp3)–H bond in the manganese-catalyzed aminations. *Org. Lett.* **2020**, *22*, 453–457. [CrossRef] [PubMed]

64. Ren, X.; Lu, Y.; Lu, G.; Wang, Z.X. Density functional theory mechanistic study of Ni-catalyzed reductive alkyne–alkyne cyclodimerization: Oxidative cyclization versus outer-sphere proton transfer. *Org. Lett.* **2020**, *22*, 2454–2459. [CrossRef] [PubMed]
65. Yang, Y.-F.; Chen, G.; Hong, X.; Yu, J.-Q.; Houk, K.N. The origins of dramatic differences in five-membered vs six-membered chelation of Pd(II) on efficiency of C(sp3)-H bond activation. *J. Am. Chem. Soc.* **2017**, *139*, 8514–8521. [CrossRef]
66. Yu, S.-Y.; Peng, X.; Wang, F.; Cao, J.; Wang, F.; Zhang, C.-G. Density functional theory study of the regioselectivity in copolymerization of bis-styrenic molecules with propylene using zirconocene catalyst. *Catalysts* **2022**, *12*, 1039. [CrossRef]
67. Lu, T.; Chen, Q.X. Realization of conceptual density functional theory and information-theoretic approach in Multiwfn program. In *Conceptual Density Functional Theory*; WILEY-VCH GmbH: Weinheim, Germany, 2022; pp. 631–647.
68. Parr, R.G.; Pearson, R.G. Absolute hardness-companion parameter to absolute electronegativity. *J. Am. Chem. Soc.* **1983**, *105*, 7512–7516. [CrossRef]
69. Parr, R.G.; Von Szentpaly, L.; Liu, S.B. Electrophilicity index. *J. Am. Chem. Soc.* **1999**, *121*, 1922–1924. [CrossRef]
70. Domingo, L.R.; Chamorro, E.; Pérez, P. Understanding the reactivity of captodative ethylenes in polar cycloaddition reactions. A theoretical study. *J. Org. Chem.* **2008**, *73*, 4615–4624. [CrossRef]
71. Parr, R.G.; Yang, W. Density functional approach to the frontier-electron theory of chemical reactivity. *J. Am. Chem. Soc.* **1984**, *106*, 4049–4050. [CrossRef]
72. Fu, R.; Lu, T.; Chen, F.-W. Comparing methods for predicting the reactive site of electrophilic substitution. *Acta Phys. Chim. Sin.* **2014**, *30*, 628–639.
73. Lu, T.; Chen, F.-W. Multiwfn: A multifunctional wavefunction analyzer. *J. Comput. Chem.* **2012**, *33*, 580–592. [CrossRef] [PubMed]
74. Humphrey, W.; Dalke, A.; Schulten, K. VMD: Visual molecular dynamics. *J. Mol. Graph.* **1996**, *14*, 33–38. [CrossRef] [PubMed]
75. Lu, T. TSTcalculator. Available online: http://sobereva.com/310 (accessed on 10 March 2023).

Disclaimer/Publisher's Note: The statements, opinions and data contained in all publications are solely those of the individual author(s) and contributor(s) and not of MDPI and/or the editor(s). MDPI and/or the editor(s) disclaim responsibility for any injury to people or property resulting from any ideas, methods, instructions or products referred to in the content.